

A novel bistable device to study mechanosensitive cell responses to instantaneous stretch

Young Choi^a, Giulia Morlino^b, Amparo Toboso-Navasa^b, Raoul Hopf^{a,c,d},
 Francesca Michela Pramotton^{a,c}, Anne Bigot^e, Andrea Taddei^b, Nikola Cesarovic^{f,g},
 Volkmar Falk^{f,g}, Edoardo Mazza^{a,c,*}, Costanza Giampietro^{a,c,d,**}

^a Department of Mechanical and Process Engineering, ETH Zurich, Zurich 8092, Switzerland

^b Benevolent AI, WIT 5HD London, UK

^c Swiss Federal Laboratories for Materials Science and Technology (EMPA), Dübendorf 8600, Switzerland

^d Senecell AG, Zurich 8057, Switzerland

^e Sorbonne Université, Inserm, Institut de Myologie, Centre de Recherche en Myologie, F-75013 Paris, France

^f Department of Health Sciences and Technology, ETH Zurich, Zurich 8092, Switzerland

^g Charité – Universitätsmedizin Berlin, Berlin 10117, Germany

ARTICLE INFO

Keywords:

Bistable device
 Uniaxial stretch
 Instantaneous stretch
 Mechanotransduction

ABSTRACT

The behavior of cells and tissues *in vivo* is determined by the integration of multiple biochemical and mechanical signals. Of the mechanical signals, stretch has been studied for decades and shown to contribute to pathophysiological processes. Several different stretch devices have been developed for *in vitro* investigations of cell stretch.

In this work, we describe a new 3D-printed uniaxial stretching device for studying cell response to rapid deformation. The device is a bistable compliant mechanism holding two equilibrium states—an unstretched and stretched configuration—without the need of an external actuator. Furthermore, it allows multiple simultaneous measurements of different levels of stretch on a single substrate and is compatible with standard immunofluorescence imaging of fixed cells as well as live-cell imaging.

To demonstrate the effectiveness of the device to stretch cells, a test case using aligned myotubes is presented. Leveraging material area changes associated with deformation of the substrate, changes in nuclei density provided evidence of affine deformation between cells and substrate. Furthermore, intranuclear deformations were also assessed and shown to deform non-affinely.

As a proof-of-principle of the use of the device for mechanobiological studies, we uniaxially stretched aligned healthy and dystrophic myotubes that displayed different passive mechanical responses, consistent with previous literature in the field. We also identified a new feature in the mechanoresponse of dystrophic myotubes, which is of potential interest for identifying the diseased cells based on a quick mechanical readout. While some applications of the device for elucidating passive mechanical responses are demonstrated, the simplicity of the device allows it to be potentially used for other modes of deformation with little modifications.

1. Introduction

The behavior of cells and tissues *in vivo* is determined by the integration of multiple biochemical and mechanical signals. Emerging literature shows that cell phenotypes are strongly influenced by external mechanical stimuli, among which stretch has contributed to physio- and pathological cellular processes including cell proliferation, migration,

differentiation, and damage [1–3]. Many different human cell types, including muscular, vascular, or gastrointestinal cells experience mechanical stretch because of their anatomical location or physiological function [4–6]. The relevancy of mechanical stretch in physio- and pathological cellular function has driven the exploration into its effects on cells requiring suitable *in vitro* devices to study them using a reductionist approach.

* Correspondence to: E. Mazza, Swiss Federal Laboratories for Materials Science and Technology (EMPA), Dübendorf 8600, Switzerland.

** Correspondence to: C. Giampietro, Empa – Materials Science and Technology, Überlandstrasse 129, CH-8600 Dübendorf, Switzerland.

E-mail addresses: mazza@imes.mavt.ethz.ch (E. Mazza), costanza.giampietro@empa.ch (C. Giampietro).

<https://doi.org/10.1016/j.bioadv.2022.213134>

Received 11 April 2022; Received in revised form 17 August 2022; Accepted 25 September 2022

Available online 28 September 2022

2772-9508/© 2022 The Authors. Published by Elsevier B.V. This is an open access article under the CC BY license (<http://creativecommons.org/licenses/by/4.0/>).

Numerous devices have been developed to stretch cells for a wide range of applications as described in previous reviews [7–9]. Each stretch device is tailored to investigate particular mechanobiological or biomechanical phenomena under different modes of tension loadings (e.g. uniaxial, shear, equibiaxial), and at different size scales, from the single-cell to collective cell behavior. Most of these devices are designed for exploring the long-term or adaptive responses to cyclic stretch, such as changes in the activation of intracellular pathways, secreted factors, or cell morphology. Studying the adaptive responses of cells has provided mechanobiological understanding of how cells react to mechanical stimuli, as well as how this process can go awry with diseases.

Cell responses vary over time and can be differentiated by time-dependence into passive or active responses. Passive responses of cells to stretch are the immediate material effects observed after stretching such as cellular elongation or instantaneous deformation dictated by the mechanical properties of the cells and their interactions. Active responses are the delayed processes after cells adapt to stretch, such as cellular reorientation towards favorable energy minima angles after cyclic stretching [10]. Delineating passive *versus* active responses is relevant to determine whether observed effects are the result of the cell as a passive material or as an active material after internal changes have surpassed. With this higher resolution of response interpretation, differences between healthy and pathological mechanical cell responses could be discerned and used as phenotypic markers for their identification.

In this paper, we describe the design and demonstrate the effectiveness of a 3D-printed uniaxial stretching device for investigating the effects of an instantaneously applied stretch on cells. In contrast to cyclic stretch devices, this set-up allows for facile visual investigations of the passive mechanical responses of cellular materials to stretch, such as how they deform instantaneously or fracture. The device is a compliant bistable mechanism [11]; this means that it can hold two stable equilibrium positions within its range of motion: a reference unstretched and stretched configuration. The compliant bistability of the device allows investigation into the effects of a rapidly applied uniaxial stretch and compatibility with standard immunofluorescence and live-cell imaging techniques. Furthermore, this stretching device allows multiple concurrent measurements of different levels of stretch on the same sample.

In addition to introducing a novel 3D-printed stretch device, we also demonstrate an application of the device to investigate the rapid stretch response of myotubes. Myotubes are multi-nucleated, elongated cells that are the major constituent of skeletal muscle. They are regularly being subjected to mechanical stimuli particularly in the form of tensile forces that beget stretches. Mechanical stretch modifies the molecular and biomechanical properties of these cells, composing an active response that is dependent on the stretching regime applied [12]. Mechanical stimulation is generally recognized as a beneficial stimulus for the maturation of skeletal muscles, but has also been known to have other direct effects on myotubes, such as changes to metabolism, secretion, maturation, and cell damage [12,13]. Duchenne muscle dystrophy (DMD) is a severe genetic disorder affecting muscle cells caused by the deficiency of the structural protein dystrophin, making them more susceptible to damage and precipitating progressive loss of muscle tissue and function [14]. Alterations have been found in the mechanical properties of dystrophic myotubes [15,16], which could be leveraged to develop a functional *in vitro* stretch assay that could elucidate mechanical differences between healthy and DMD myotubes.

We use the novel set-up to investigate differences between healthy and DMD myotubes, and we provide a proof-of-principle of our cell-stretching device for mechanobiological studies. Moreover, we identify a new phenotypic characteristic of DMD myotubes that could potentially be used, in combination with this device, as a readout for the screening of promising candidate compounds for drug development.

2. Materials and methods

2.1. Description of device design

The bistable stretching device consists of two main components (Fig. 1A): 1) the 3D-printed body, and 2) the deformable polydimethylsiloxane (PDMS) substrate. The 3D-printed body (length \times width \times height, 70.4 \times 51.8 \times 4.0 mm) has a specific geometric design that provides the bistable characteristic of the device, which was inspired by previous work [11]. Specifically, the body contains four rigid elements that elastically deflect at their ends, creating a latching mechanism that strictly limits a one-dimensional movement of the moving member and stably hold two configurations. Once a small threshold displacement is applied to the moving member, in this study – by applying force by hand, it rapidly shifts from one configuration to the other. The overall displacement of the moving member can be tuned by proportionally scaling the length of the rigid elements.

The second major part of the device is the PDMS substrate, on which cells adhere. Four posts (height \times diameter, 3.0 \times 2.3 mm) are situated on top of the 3D-printed body: two located on the moving member of the device and two on the non-moving frame. The deformable PDMS substrate is mounted onto the posts via specific holes cut in the substrate. 3D-printed caps (length \times width \times height, 10 \times 5 \times 4.3 mm) are dimensioned to be press-fit over the posts to secure the substrate in place. There is a 300 μ m distance between the bottom of the caps and 3D-printed body when lowered to constrain out-of-plane deformations while not compressing the PDMS substrate at the fixation points. There are two symmetric raised 0.4 mm regions on top of the frame to accommodate the placement of a glass coverslip over the substrate. A small clearance (approx. 100 μ m) between the glass coverslip and the substrate permits addition of a thin fluid layer of mounting medium for fluorescent microscopy imaging. The local stretches that the cells experience can be tuned by modifying the geometry of the substrate.

The PDMS substrate (length \times width \times height, 30.0 \times 10.0 \times 0.300 mm) is geometrically designed so a range of different levels of stretches can be evaluated by examining different regions on the same sample. The levels of strain on each substrate are determined through finite element (FE) model simulations and validated by DIC measurements. A 3D-printed immunostaining well, a separate component not part of the bistable stretching device but integral to the overall procedure, is designed to minimize fluid volume necessary to quench the stretched substrate in either fixation or immunostaining cocktail solutions.

2.2. Description of general stretching experimental procedure for immunostaining

A detailed schematic diagram of the stretching procedure for immunostaining is shown in Fig. 1B. In summary (detailed descriptions of steps follow in later sections), cells are seeded and expanded on the substrates inside of a cell culture dish. For stretching, each substrate is mounted onto the 3D-printed body in the unstretched configuration. 3D-printed caps are pressed onto the posts until fully engaged. Once the substrate is secured onto the device, it is actuated by hand to initiate the stretching episode. The device in its stretched configuration is then immediately transferred onto a 3D-printed immunostaining well filled with pre-warmed fixation solution. After immunostaining, substrates are imaged using fluorescence microscopy at specific regions corresponding with different stretch levels. It should be noted that for this application unstretched and stretched substrates were not the same sample.

2.3. Description of experimental procedure for live-cell imaging

Cells were seeded and cultured on substrates as reported in Sections 2.9 and 2.10. On the day of the experiment, cell culture medium was removed, and cells were treated with Hoechst 33342 staining solution in PBS^{+/+} (1:2000, #62249, Thermo Fisher Scientific) in the incubator for

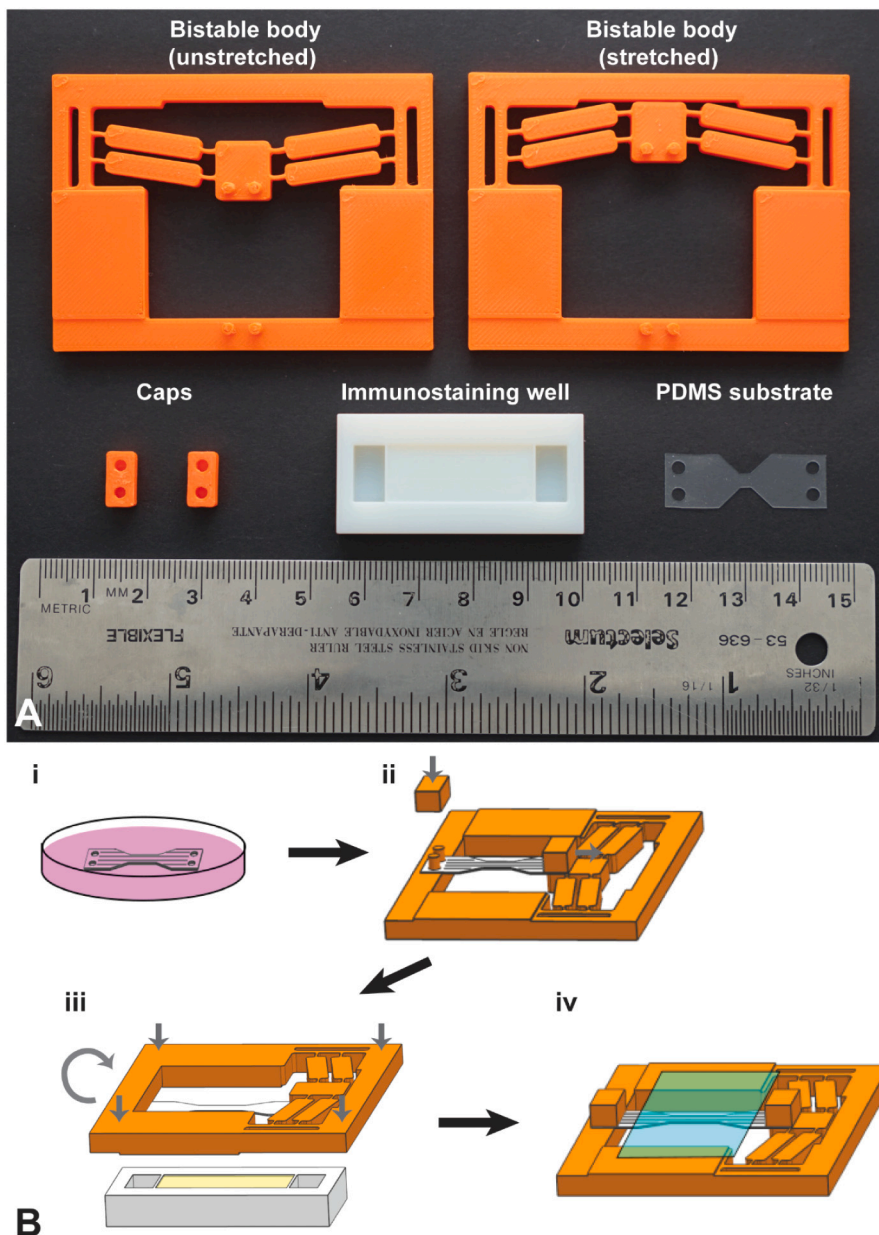


Fig. 1. Photos of the bistable stretch device and procedural flow diagram of uniaxial stretch experiments for immunostaining imaging. A) Photo of each component of the bistable stretching device including the 3D-printed bistable body (in both the unstretched and stretched configuration), caps, immunostaining well, and PDMS substrate. B) Flow diagram showing the procedural steps for stretching aligned adherent cells, described as follows: i) Cells cultured on micropatterned substrates created with a microstamping process to align cells; ii) PDMS substrate with cells mounted onto the bistable stretching device, caps placed on top of posts to secure the substrate, and stretching actuated by pressing device forward by hand; iii) stretched device placed into the immunostain well for fixation and subsequent immunostaining immersion steps; iv) glass coverslip placed over the immunostained cells as preparation for fluorescent microscopy imaging.

10 min. After 3 washes with PBS^{+/+}, substrates were mounted onto the bistable stretching device. Three regions were marked on the backside of the substrate (side without cells) with a fine tipped pen to visualize the same regions and identify the same cell nuclei before and after stretching. The stretch device was then returned to prewarmed PBS^{+/+} and regions of interest were imaged in the unstretched configuration. Then device was stretched, and each region was immediately imaged again in the stretched configuration.

2.4. Fabrication of 3D-printed components

Computer-aided designs (CAD) of each 3D-printed component were made using NX 12 (Siemens). The 3D-printed body and caps were printed using an I3 MKS+ 3D printer (Prusa Research) and polylactic acid (PLA) biopolymer filament (Prusa Research) [17]. Print parameters were 0.20 mm layer height thickness and 20 % infill volume. The immunostaining wells were fabricated using a Polyjet 3D printer (Stratasys) with VeroWhite material (Stratasys). All CAD files will be provided upon reasonable request.

2.5. Fabrication and preparation of deformable PDMS substrates

PDMS (Dow Corning, Sylgard 184) sheets with a thickness of 300 μ m were produced as previously reported [18]. Briefly, PDMS sheets were created using a 10:1 ratio mixture of base to crosslinker, degassed in a vacuum chamber, and cured in-between two glass plates separated by spacers of 300 μ m thickness. PDMS sheets were cut into individual substrates using a laser cutter (Speedy 100, Trotec) with the following settings: 8 laser power, 1 cutting velocity, and 1000 pulse frequency. The surface of each substrate was cleaned and sterilized as follows: using tape to remove the large particles, immersion into an ultrasonic bath filled with 70 % ethanol for 10 min, then drying under UV light.

2.6. PDMS substrate design and finite element model

The FE model was made in Abaqus (Abaqus/CAE 2018, Dassault Systemes). It was used to calculate the deformation of the PDMS substrates and refine the geometry to obtain adequate magnitudes as well as ranges in the local deformations. All deformation measurements are

reported as strains or stretch, calculated as:

$$\varepsilon = \frac{\text{stretched length} - \text{original length}}{\text{original length}}$$

$$\lambda = \varepsilon + 1$$

By default, the ε_{11} strain component, which is parallel to the direction of applied stretch, is solely referred throughout the paper to designate the corresponding deformation in specific regions of interest on the substrate. The specific strain component will be explicitly stated in any other case (i.e. ε_{22} , the strain perpendicular to the stretch direction).

The FE model was 2D-planar, quarter-symmetric with 3.5 mm displacement applied to the outer semicircle of the hole matching the experimentally measured nominal displacements from digital image correlation (DIC). 4-node, quadrilateral plane stress elements with reduced integration and large-strain formulation were selected. A PDMS constitutive model based on previously performed multiaxial large strain mechanical experiments was applied for all simulations [19].

2.7. Digital image correlation and experimental strain measurements

The displacement field for the stretched substrates was acquired using DIC. Random speckle patterns were drawn onto sample substrates with a fine tipped pen (Fig. 3A). Images of the unstretched and stretched configurations of the same substrate were taken using an EO-2323 M camera (Edmund Optics, Inc.). To verify the reproducibility of the device to generate similar strains, the DIC experiment was independently repeated four times ($n = 4$). Manual measurements of the nominal (global) strains were calculated by tracking displacements of the moving capped member relative to the fixed non-moving cap on the frame of the bistable mechanism from the scaled images of the reference and stretched configurations using ImageJ (<https://imagej.nih.gov>). The overall strain field on the substrate was calculated using NCorr software [20].

To measure the displacement rate, the actuation of the device was recorded using a mounted camera at 120 fps. The displacement of the marked point on the moving cap on the stretching device was tracked using Kinovea software (<https://www.kinovea.org>).

2.8. Micro-structure wafer and microprinting stamp preparation

Micro-structures on a silicon wafer were used to create microprint stamps to selectively attach fibronectin onto the PDMS substrates to align cells parallel to the stretch direction. First, template wafers with gratings of 75 μm depth and 50 μm width were fabricated at the cleanroom facilities of the Binnig and Rohrer Nanotechnology Center (BRNC) using a standard photolithography process [21]. The silicon wafers were then passivated as follows: soaking for 30 min in a silanization solution I (Sigma-Aldrich, USA), 10 min in hexane (Sigma-Aldrich, USA), 10 min in 1-octanol (Sigma-Aldrich, USA), and rinsed with acetone and deionized water.

Stamps used for microprinting were created by pouring a degassed PDMS (Dow Corning, Sylgard 184) in a 10:1 mixing ratio onto the micro-structured wafer, which was then cured in an oven at 80 °C for 2 h. PDMS was carefully removed from the silicon wafer and left overnight to fully cure at room temperature (RT). Individual 30 × 10 mm stamps were cut from the larger PDMS strip pad. Stamps were cleaned for 10 min with 70 % ethanol in an ultrasonic bath, air dried under cell culture hood, and sterilized under UV light before usage.

2.9. Fibronectin microcontact printing coating

Using a sterile micropipette tip, the stamp surface was coated with an 8 $\mu\text{g}/\text{ml}$ fibronectin (FN; F1141 Sigma Aldrich) solution in PBS in a cell culture hood. The solution was dragged over the entire stamp until the

highly hydrophobic surface was quenched in solution. The stamps were then placed in an incubator for 30 min at 37 °C. Individual PDMS substrates (print surface) were cleaned with 70 % ethanol for 10 min and oxygen plasma treated (80 watts for 60 s, 1 ± 0.2 mbar) to increase their hydrophilicity. The stamps were removed from the incubator and pressed firmly onto the plasma treated PDMS substrates for 30 s, then rinsed gently with PBS.

2.10. Cell culture

Immortalized healthy (AB1190) and Duchenne Muscular Dystrophy (DMD, AB1324) human myoblasts were obtained from Vincent Mouly [22]. Cells were routinely cultured in skeletal muscle cell growth medium (C-23160, Promocell) and split at 60 % confluency. Myotube differentiation was induced at confluence by replacing the growth medium with DMEM supplemented with 100 $\mu\text{g}/\text{ml}$ transferrin (Sigma-Aldrich), 10 $\mu\text{g}/\text{ml}$ insulin (Sigma-Aldrich), and 50 $\mu\text{g}/\text{ml}$ of gentamycin (Sigma-Aldrich) for 2 days.

2.11. Immunofluorescence

Cells were fixed with 4 % paraformaldehyde (PFA) in PBS for 20 min at RT, permeabilized for 10 min with PBS 0.5 % Triton-X and incubated for 1 h at RT in a blocking solution of PBS with 5 % Bovine Serum Albumin. Samples were then incubated with primary antibodies diluted in blocking solution overnight at 4 °C, washed with PBS, incubated with appropriate secondary antibodies and DAPI for 1 h at RT, mounted with Fluoroshield Mounting Medium (Sigma-Aldrich) and imaged.

2.12. Antibodies

The following primary antibodies were used for immunofluorescence: mouse monoclonal anti-YAP/TAZ (1:100, #sc-101199, Santa Cruz Biotechnology Inc.), mouse monoclonal anti-Myosin-4 (MF20) (1:100, #14-6503-82, Thermo Fisher Scientific), rabbit polyclonal phospho-paxillin Y31-Y118 (1:100, #2541, Cell signaling) and mouse monoclonal anti- β 1-integrin (1:100, ab30394, Abcam). The secondary antibodies were donkey anti-mouse Alexa Fluor 555 (1:200; #A31570, Thermo Fisher Scientific), donkey anti-mouse Alexa Fluor 647 (1:200, #A31571, Thermo Fisher Scientific), and chicken anti-rabbit Alexa Fluor 647 (1:200, #A21443, Thermo Fisher Scientific). Cell nuclei were stained with DAPI (1:1000, #62248, Thermo Fisher Scientific).

2.13. Image acquisition

Immunostained samples were imaged using an inverted Nikon-Ti spinning disk confocal microscope (Nikon, Japan) equipped with a DU-888 camera (Oxford Instruments, United Kingdom) and a pE-100 LED illumination system (CoolLED Ltd., Andover, United Kingdom). A 20 \times , 0.75 numerical aperture (NA) air objective (Plan Apo, Nikon, Japan) was used. Larger 1865 × 1865 μm^2 images were acquired of specific regions that corresponded to different levels of strain (calculated from FEM and DIC results) by stitching multi-point images with 20 % overlap together. For example, for immunofluorescence image analysis (Myosin-4 and YAP/TAZ), images at the center of the stretched substrate and 5 mm left or right (in the stretch direction, Fig. 2C) were captured, which corresponded to approximately 30 % and 20 % strain, respectively. Adjustments to brightness and contrast were only made in the preparation of the figures. For comparison purposes, different sample images of the same antigen were acquired under constant acquisition settings.

Live-cell imaging was performed using an inverted ZEISS Axio Vert. A1 microscope (ZEISS) equipped with a ZEISS AxioCam 105 colour camera and DAPI filter (ZEISS). A 10 \times , 0.25 NA objective (ZEISS) was used. Brightfield images were taken to capture marker (substrate) deformation and DAPI filtered images were taken to capture Hoechst-

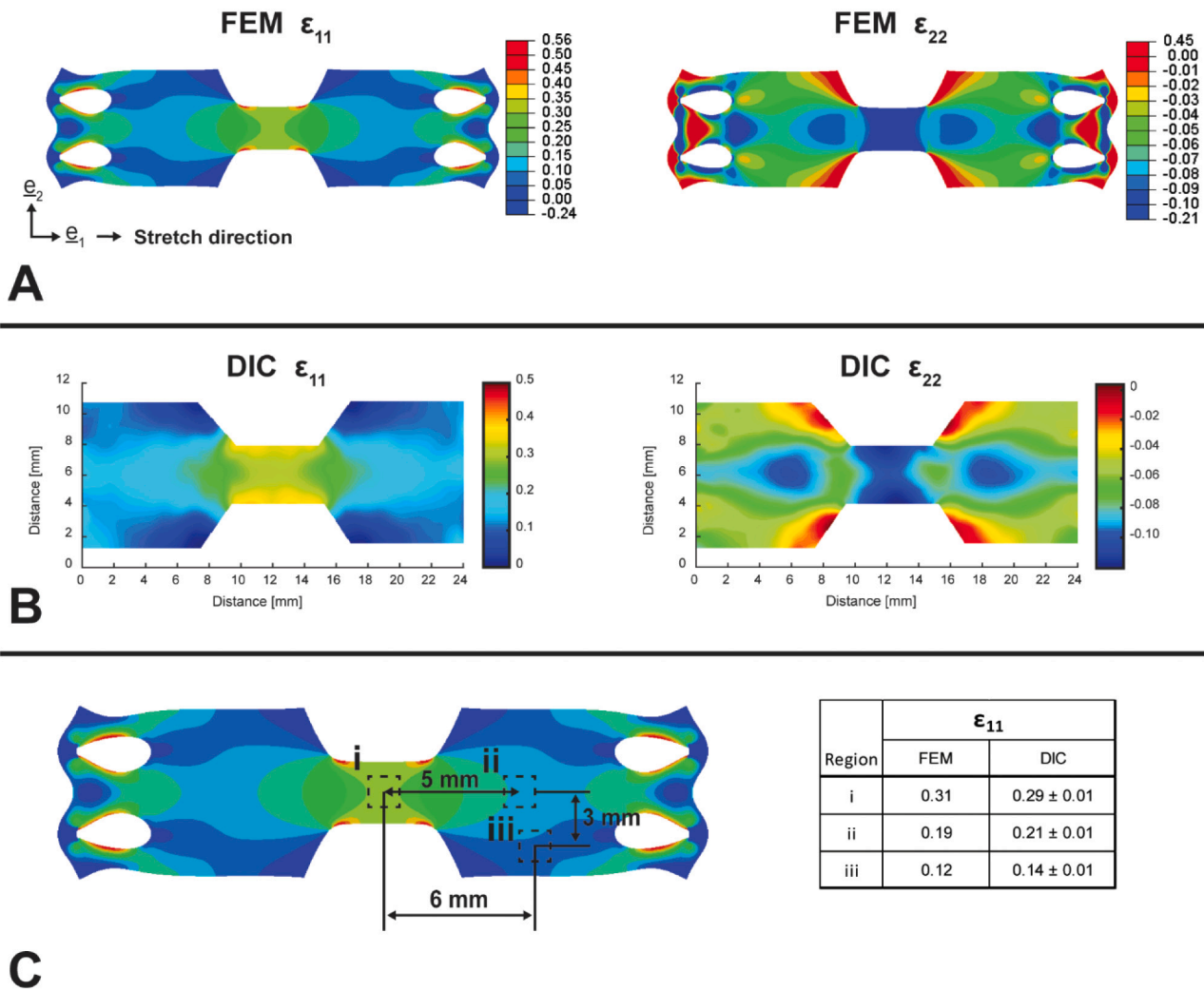


Fig. 2. FE model simulation and DIC measurements of the engineering strains on the PDMS substrate. A) Abaqus FE model simulation results for ϵ_{11} (engineering strain parallel to the stretch direction) shown on the left and corresponding FE model simulation results for ϵ_{22} (engineering strain perpendicular to the stretch direction) shown on the right. B) DIC results validating FE model simulation results for ϵ_{11} and ϵ_{22} . Similar magnitudes and distribution of strains are shown, suggesting close correlation between simulated and experimentally measured results. C) Image depicting regions that were imaged on the substrate corresponding to different ϵ_{11} levels (left) with the FE model and DIC values for each region shown in the table (right). The mean \pm standard deviation is shown for the DIC measured ϵ_{11} for independent experiments ($n = 5$).

stained nuclei deformations.

2.14. Image analysis

Customized automated segmentation scripts were developed for segmentation of nuclei (DAPI or Hoechst), myotubes (Myosin-4 positive), and YAP/TAZ nuclear localization. Nuclei segmentation was performed on nuclei stained images with the following settings on QuPath software [23]: requested pixel size = $0.5 \mu\text{m}$, background radius = $10 \mu\text{m}$, sigma = $5 \mu\text{m}$, min area = $80 \mu\text{m}^2$, max area = $400 \mu\text{m}^2$, threshold = 1000, and cell expansion = $0 \mu\text{m}$. Nuclei segmentations were exported from QuPath to ImageJ (<https://imagej.nih.gov/ij/>) for nuclei cell count and aspect ratio measurements.

For live-cell experiments, local substrate strains were calculated from tracking the displacement of three landmark points around the contour of the marker on the substrate before and after stretching (Supplementary Fig. 1A). Intra-nuclei strains, or the strains based on displacements between neighboring nuclei, were similarly calculated by manually identifying the identical segmented nuclei before and after stretch, which provided displacement field for each nucleus (Supplementary Fig. 1A). Using a Delaunay triangulation to connect landmark

points or nuclei centroids, the ϵ_{11} was calculated as the first principal stretch from the deformation gradient [24].

Myosin-4 positive cell segmentation was performed using an Image J macro on Myo-4 channel images: 1) Gaussian blur ($\sigma = 5$ pixels), 2) thresholded using a set value. Threshold values were determined automatically from surveying histograms for images belonging to the same experimental groups. When image artifacts were present, manual threshold values were selected.

To evaluate YAP/TAZ nuclear localization, nuclei segmentations were used to determine the mean intensities of the YAP/TAZ signal within the overlapping nuclear region. Briefly, because of the nuclear segmentation, a closed polygon was obtained marking the boundary of each nucleus. To approximate an area of the cytoplasm, the nucleus was enlarged using a simple geometric algorithm. In a first step the center point S was calculated as the mean value of all corner point coordinates p_i . Then the average distance r_m from the center point S to all corner points p_i was evaluated. All polygonal corner points of the enlarged nucleus q_i were then obtained by shifting each point p_i along the line that connects p_i with S, outwards by the constant distance $\alpha \cdot r_m$. In this case the distance multiplier α set to 0.5. This choice of α was able to provide a representative section of the cytoplasmic area, without

causing any measurable bias due to accidental intersections with the neighboring nuclei.

Then a growth function was applied to the nuclei segmentation to define a region of fixed size outside of the nucleus that was defined as the cytoplasmic region, where cytoplasmic boundaries were estimated via F-actin channel to ensure appropriate sizing. The mean YAP/TAZ intensity for this cytoplasmic region was also calculated. The ratio of average nuclear and cytoplasmic YAP/TAZ signal intensity was then calculated and reported as a measure of nuclear localization.

All imaging scripts and segmentation outputs can be provided upon request.

2.15. Western blotting

Western blot analysis was performed according to standard protocols. Cells were lysed in boiling Laemmli sample buffer [(2 % SDS, 20 % glycerol, and 125 mM Tris-HCl (pH 6.8)]. Protein concentration was determined using a BCA Protein Assay kit (Thermo Fisher Scientific). Equal amounts of proteins were loaded on a gel, separated by SDS-PAGE and transferred to a Protran Nitrocellulose Membrane (Whatman). After blocking and incubation with primaries (mouse anti-paxillin, 1:1000, #610051, BD Transduction Laboratories™; rabbit anti-phospho-paxillin Y31-Y118, 1:1000, #2541, Cell signaling) and horseradish peroxidase-linked secondary antibodies, specific bindings were detected using a chemiluminescence system (GE Healthcare). Western blot bands have been acquired with ChemiDoc™ MP System (Biorad) and quantified using the optic densitometry software Image Lab™ (Biorad) and normalized to the levels of an appropriate housekeeping protein.

2.16. Statistical analysis

Statistical analysis was performed using GraphPad Prism 8. Datasets were first tested for normal distribution using the Komogorov-Smirnov test. Data showing normal distributions were analyzed using parametric tests, *i.e.*, unpaired Student's *t*-test or one-way ANOVA followed

by Fisher's least significant difference (LSD) post-hoc test. Non-normal data were analyzed using non-parametric Kruskal-Wallis test with Dunn's multiple comparisons. A *p*-value of 0.05 was used for determining significant differences. For each plot, the statistical test applied, as well as *n*-values, is specified in the corresponding caption.

3. Results

3.1. Characterization of the stretching device

To characterize the local or cell-scale strains on the substrate, DIC measurements and FE model simulations were performed (Fig. 2). FE model simulations depicted a range of strains across the substrate, with higher levels strain at the center of the substrate ($\epsilon_{11} = 0.31$) that gradually decreased towards the side of the substrate (5 mm from the center $\epsilon_{11} = 0.19$). DIC experimentally measured values showed close correspondence to FE model results with $\epsilon_{11} = 0.29 \pm 0.01$ (mean \pm standard deviation) at the central region and lower strains at the side region $\epsilon_{11} = 0.21 \pm 0.01$. FE model and DIC calculated strains also showed close correspondence in strain distributions over the entire substrate, as evidenced by mirrored distributions in the colour mapped strain fields, validating FE model results.

The displacements of the moving member with respect to time were experimentally measured (Fig. 3) to describe the strain rates of the device. In the experiments, variation in time duration for the initial loading phase were from <1 s to >2 s, so to cover the range of possible durations in experiments. Most of the displacement occurs at a high displacement rate determined by the elastic deflection and stiffness of the device. Once a threshold displacement of about 1.5 mm was surpassed, the device deflected, and the remaining actuation occurred in 0.22 ± 0.03 s. This rapid actuation that is dictated by the bistable mechanism equated to a maximum nominal strain rate of 6900 ± 800 %/s, with a high level of repeatability in different experiments.

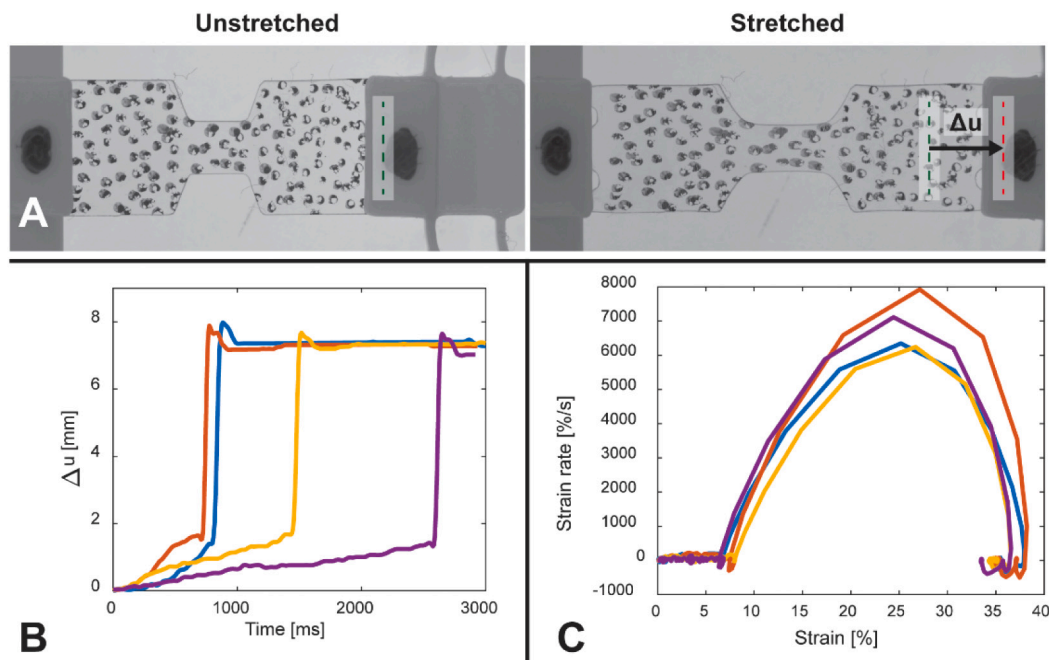


Fig. 3. A) Representative DIC images indicating how the nominal displacement of the cap on the moving body (Δu) was measured during the actuation episode. B) Plot showing Δu -time curves with each curve representing an independent experiment ($n = 4$). The beginning phase of the curve shows the loading phase when the moving body is pushed by hand. The variation in time duration for loading phases was intentional to highlight that once a certain threshold displacement was reached, the elastic deflection/mechanical properties of the device completely determine the rate and extent of displacement regardless of the initial loading phase. C) Corresponding strain rates-strain for each experiment.

3.2. Differentiation and alignment of myotubes *in vitro*

The differentiation of skeletal muscle cells *in vitro* has been well established, mirroring the *in vivo* situation in some respects including the fusion of myoblasts into myotubes [25]. It has been previously reported that microcontact printing alignment of the myoblasts favors their further differentiation [26]. In order to obtain optimal myotube differentiation, healthy and DMD myoblasts were cultured for three days and then differentiated for 2 days on FN microcontact printed PDMS substrates. Both healthy and DMD myoblasts differentiated into aligned myotubes (Fig. 4) as shown by their coordinated alignment and by the positivity for the Myosin-4 antibody, which recognizes the heavy chain of myosin II—a marker of differentiated myotubes.

3.3. Deformation of cells and nuclei in response to stretch

To evaluate for deformation propagation from the substrate to the cells, aligned healthy cells were subjected to instantaneously applied stretch. The deformation state of an incompressible material under uniaxial tension is well-defined (Fig. 5). Since the same microscopic image size is analyzed for regions of interest on the unstretched and stretched substrates, a noticeable decrease in mean cell density, or correspondingly—nuclei density, is expected. Considering a 15 % strain, the area change would equate to a 7.5 % increase in the material's area, which equates to 7.5 % lower nuclei density for a fixed image size. Based on this principle, we sought to verify the hypothesis of decreasing nuclei density in response to higher levels of stretch as confirmation that the substrate stretches are physically transferred to the cells.

Based on the locally calculated ε_{11} strain from DIC measurements of different regions on the stretched substrates, the expected value in nuclei density change corresponding to the respective levels of stretch in the imaged area were calculated. These expected values and the actual measured nuclei densities are plotted in Fig. 5. The expected nuclei density of the 15 % strain condition (695.6 nuclei/mm²) fell within the standard deviation range of the measured nuclei density (651.9 ± 47.3 nuclei/mm²), which is representative of the nuclei density variability between replicate experiments. At higher levels of stretch such as the 30 % strain condition, the expected value (604.3 nuclei/mm²) is much greater than the measured nuclei density (513.8 ± 55.6 nuclei/mm²). Visual inspection of the high strain images showed evidence of cells detaching from the substrate in the form of retracted bulbous ends of cells with high contrast edges similar to previous reports of cell peeling [27], accumulated masses of cellular material from nearly completely

detached cells, and general scarcity of nuclei in these areas (Fig. 5B). Thus, cell detachment explains the differences between measurement and expectation.

To further evaluate deformation propagation from the substrate to the cells, a live-cell experiment was performed to track the displacement of individual nuclei before and after stretch. Close correspondence between the substrate and internuclei strains was found (Supplementary Fig. 1B). The results indicate that the cell layer and substrate deformations match for all regions considered, with strain ranging from 13 % to 38 %. This correspondence confirms that the deformation is transmitted from the substrate to the cell layer.

For biomolecular evidence supporting deformation transfer, immunostaining of focal adhesions, the mechanical link between the cell and substrate, was performed. The presence of focal adhesions was observed in both unstretched and stretched samples, as depicted by the phosphopaxillin and β 1-integrin markers (Supplementary Fig. 2).

In addition to the nuclei density, nuclei aspect ratio was also evaluated for deformation transfer on a sub-cellular scale. It was established that stretch-induced changes occur in nuclear shape and are mostly passive events [28,29]. Despite a slight increasing trend in nuclei aspect ratio in response to increasing strain, the expected aspect ratio change assuming affine deformation—i.e., uniform transfer of local substrate deformations directly to the nuclei—is much larger than the observations, suggesting a non-affine deformation for the cell nuclei. Further discrepancies between nuclei and affine deformations can be found from the live-cell experimental data tracking the relative change in aspect ratio of the same nuclei before and after stretch (Fig. 6B). While there is still a tendency for aspect ratio to be increasing (11 % median change at 38 % strain), there is a far less change than would be expected for an affine nuclear deformation (62 % median change).

3.4. Detachment of healthy vs DMD myotubes

With evidence of healthy myotube detachment following rapid stretch, we investigated whether similar signs of detachment would be found with the dystrophic myotubes. As shown in Fig. 7 panels A and B, early stretch-induced detachment of myotubes was different between the two cell types. Healthy myotubes underwent a fast and significant detachment from the substrates at the 20 and 30 % strain levels, highlighted by the significant reduction in percentage of Myosin-4-positive cells from the unstretched control condition. On the contrary, DMD myotubes withstood identical levels of stretch with negligible detachment, as shown by the elongation of their cell bodies and retention of

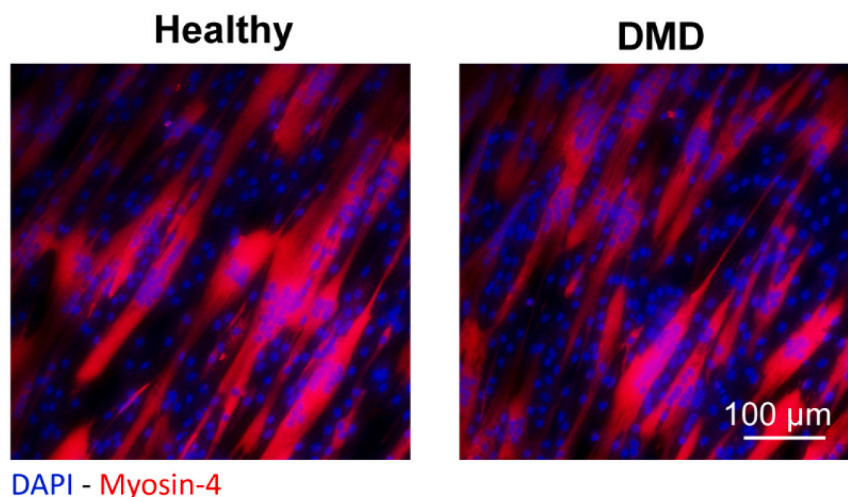
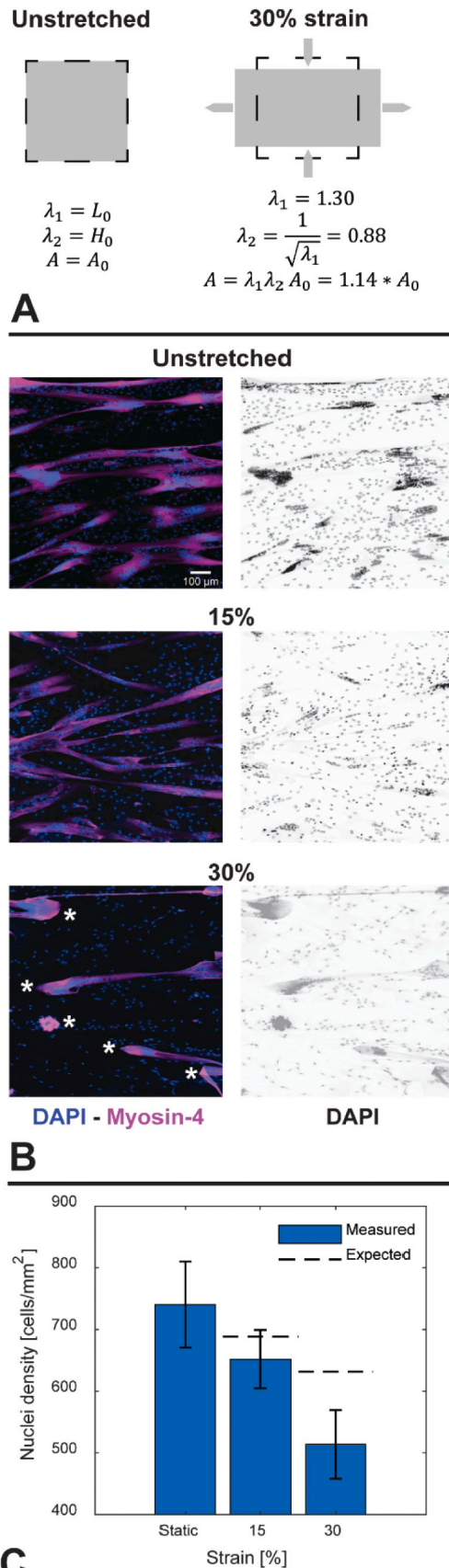


Fig. 4. *In-vitro* myotube differentiation of healthy and dystrophic cell lines. Representative immunofluorescence staining of Myosin-4 (red) in aligned healthy and DMD myotubes after induction of differentiation *in vitro*. Nuclei are counterstained with DAPI (blue). Images depict positive alignment and similar cell myotube density with employed culturing procedures.



(caption on next column)

Fig. 5. A) Diagram depicting the material area change that occurs under an idealized 30 % uniaxial strain with contraction, which is the state of deformation expected in the center of the substrate. Identical sized image areas are sampled from both unstretched and stretched substrates, and therefore, the microscopic images capture a smaller material area in respect to the unstretched case since the material has increased in area. B) Immunofluorescent images of healthy muscular cells at the unstretched, 15 %, and 30 % strain conditions. The left column shows composite images with Myosin-4 (magenta) and DAPI (blue) stained cells, while the right column shows only the DAPI stained channels. Cells elongate with the substrate at 15 % strain (middle row), but signs of myotube detachment are evident at 30 % strain (bottom images, i.e. bulbous ends with high contrast, condensed matter in middle of image, snapped back ends of cells marked with asterisk *). C) Bar graph showing the change in nuclei density depending on the strain condition. The measured means and standard deviations are shown from independent experiments ($n = 3$). The dashed lines indicate the expected value for nuclei density based on the area change and mean unstretched nuclei density. The expected nuclei density at 15 % strain falls within the standard deviation range of the measured values. At 30 % strain, the expected value is far larger than the measured because of cell detachment.

myosin-4 positive percent area. It has been previously reported in an *in vivo* *mdx* mouse, the most common animal model of DMD, that a strong upregulation of focal adhesion proteins in the muscle occurs, including the phosphoprotein paxillin [30]. This prompted us to hypothesize that the reduced detachment of DMD myotubes could be a consequence of an increased level of adhesion proteins occurring also in our *in vitro* model. It was then confirmed by western blot analysis that in both DMD myoblasts and myotubes paxillin levels were higher, as well as its phosphorylation at Y31 and Y118 compared to the healthy counterpart, supporting the hypothesis that the higher tolerance to stretch could be attributed to stronger focal adhesions (Fig. 7C).

3.5. Confirmation of differences in nuclear YAP-TAZ between healthy and DMD cells

YAP and its homolog TAZ, the Hippo pathway effectors, are key mechanotransducers sensing mechanical stimuli and relaying signals to control multiple transcriptional programs [31]. Mechanical cues such as cell stretch have been identified as regulators of YAP/TAZ nuclear translocation and activity. Mechanical stretching is sufficient to induce the entry of YAP/TAZ into the nucleus [32] for many cell types including myoblasts *in vitro* [33], and mature skeletal muscle fibers *in vivo* [34]. However, in the *mdx* mouse (popular *in-vivo* mouse model of DMD), contractile loading does not induce YAP nuclear relocalization as the basal level is already elevated. We thus tested if we were able to recapitulate *in vitro* this defective behavior of YAP/TAZ nuclear translocation observed *in vivo* with our device and experimental setup.

Through immunofluorescence analysis, we showed that *in vitro* stretching of healthy cells induced a non-significant but increasing trend in nuclear YAP/TAZ relative to cytosolic levels that directly correlates with the amount of the stretch applied. DMD cells showed a constitutive higher YAP/TAZ nuclear localization compared to the healthy counterpart at unstretched conditions with no significant changes or noticeable trends in response to load (Fig. 8). These data suggest altered mechanotransduction of DMD cells *in vitro*, where a basal higher level of active YAP/TAZ in the nucleus (unstretched condition) could impair the proper response to load.

4. Discussion and conclusions

We have introduced and described the design of a 3D-printed bistable stretch device for mechanobiological study applications. Consisting of few parts that are all easily modifiable using rapid fabrication techniques, such as 3D printing and lasercutting, it coalesces into a device that offers one major benefit – simplicity. Akin to other 3D-printed stretch devices [35–39], fabrication of this device is low-cost

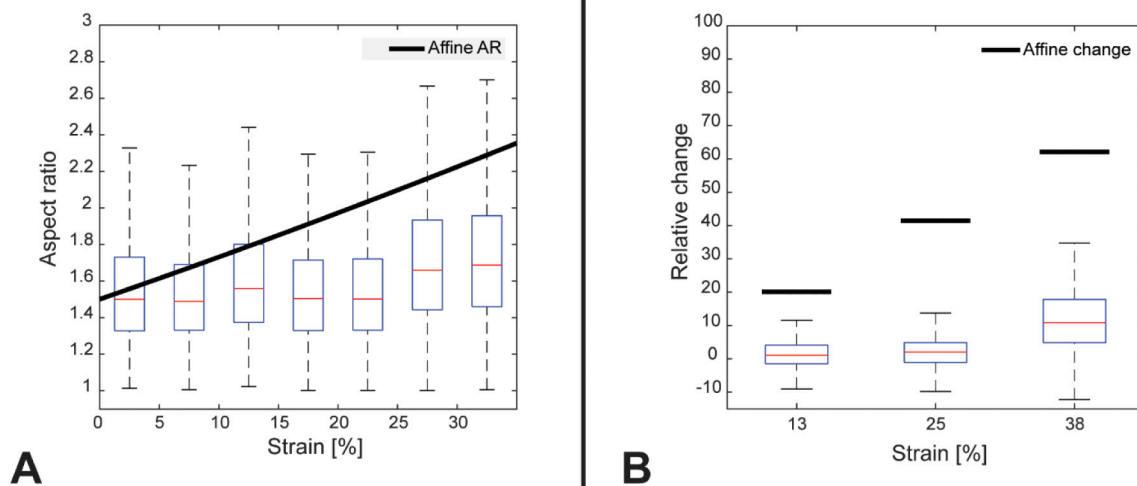


Fig. 6. A) Box plots showing nuclei aspect ratio (AR) of healthy muscular cells in response to different levels of strain that are binned in 5 % strain intervals. The black line indicates the nuclei aspect ratio change assuming affine nuclear deformation based on the median aspect ratio of the 0–5 % strain interval: $Affine\ AR = (median\ AR@0 - 5\%Strain) * (1 + strain) * \sqrt{1 + strain}$. B) The relative change in aspect ratio of the same nuclei before and after stretch at different strain levels from live-cell experiments is shown. The solid bar indicates the relative change in nuclei aspect ratio assuming affine deformation based on the median unstretched aspect ratio (13 % $n = 346$; 25 % $n = 561$ and 38 % $n = 306$). For the case of 38 % strain: $Affine\ change = (median\ AR@unstretched) * (1 + .38) * \sqrt{1 + .38}$. Both the increase in aspect ratio at different strain levels and the relative change in aspect ratio is less than what would be expected for a perfectly affine intranuclear deformation.

and fast. Specifically, a single bistable device utilizes 8.69 g of PLA filament costing \$0.22 in total and is completed in less than an hour. The simplicity of the device's design is extended to its actuation mode as a compliant mechanism, or bistability characteristic, which removes the necessity for bulky and more complex actuation systems to drive the stretching. Further, lasercutting of PDMS substrates provides an efficient method for producing highly reproducible geometries of complex 2D structures, or even 3D substrate geometries [40].

The device can reliably produce a distribution of strains on a single substrate, providing multiple simultaneous experimental conditions in specific regions of the substrate. These strain distributions are both tunable and scalable by either: 1) changing the nominal displacement applied to the substrate ends by modifying the 3D-printed body design, or 2) changing the geometry of the substrate. The FEM model that was verified using standard DIC techniques produced accurate simulations of the local strains. By employing the FEM model and simulating any modifications to the design parameters of the device, a large variety of different strain conditions can be realized within the limits of the deformability of materials used.

Unlike existing cell stretch devices, the set-up presented here is uniquely adapted for applying a controlled rapid stretch onto cells for investigations of the instantaneous or short-term effects of mechanical stretch. Recently, a stretching device for rapid stretch of cells was described with strain rates up to 170 %/sec that uses an external pneumatic actuation system [41]. Our device has a peak strain rate of about 7000 %/sec (see Fig. 3C) and can be operated by hand. The stretching episode is completed in less than a second after which the cells are immediately fixed, with this entire process taking about 5 s. Since the kinetics for cell reorientation in response to stretch is approximately 100 s [42], and turnover of focal adhesions and cytoskeletal actin components in the order of 10s [10,43,44], we assume that the device provides insight into the acute effects of stretch on cells before such active or adaptive mechanisms can respond. The acute stretch of the substrates on which cells are seeded triggers cell behaviors that cannot be identified in the usual static tissue culture environment and can provide evidence of features of mechanotransduction associated

with pathological situations.

We demonstrated that substrate deformations were transferred to the cells through noticeable reductions in nuclei density with increasing strains, integrity of focal adhesion components of unstretched and stretched cells, and close correspondence between internuclei and substrate strains through live-cell experiments. Cells adhere to underlying substrates via transmembrane adhesion proteins known as integrins, which allows the cell layer to deform globally in the same way as the substrate.

At the cell level, reductions in cell nuclei density related to material area changes of the local deformation states provided supporting evidence that forces are propagated to the cell layer from the substrate, leading to coordinated deformations of the cell with the substrate. At low strain levels (<15 %), nuclei density reductions fell within the expected amounts indicating affine deformations, or in other words, that the local strains on the substrate matched those on the adhered cell layer. Beyond this strain value (>15 %), larger reductions in nucleus numbers were observed due to detachment of cells. Live-cell experiments allowed tracking the displacement field of individual nuclei, indicating affine deformation of the cell layer with respect to the substrate for strains up to 38 %.

At the nuclei level, deformation was apparent as nuclei aspect ratio in average slightly increased with strain, but the magnitude of this change was far lower than expected, demonstrating non-affine nuclei deformations. Studies have revealed vimentin intermediate filaments and LINC (linker of nucleoskeleton and cytoskeleton) complexes to connect the cell nucleus directly to the cytoskeletal network [45]. Through these cytoskeletal connections, substrate deformations can be transferred to the nucleus. On the other hand, the nuclear envelope is reported to be a network with higher stiffness than the plasma membrane, and act as a 'molecular shock absorber'. [46] This mismatch in stiffness between the nucleus and surrounding cell body could contribute the observed non-affinity.

To demonstrate how the device can be used to find mechanical differences *in vitro* between healthy and pathological cell types, a comparison between stretched healthy and DMD myotubes test case was

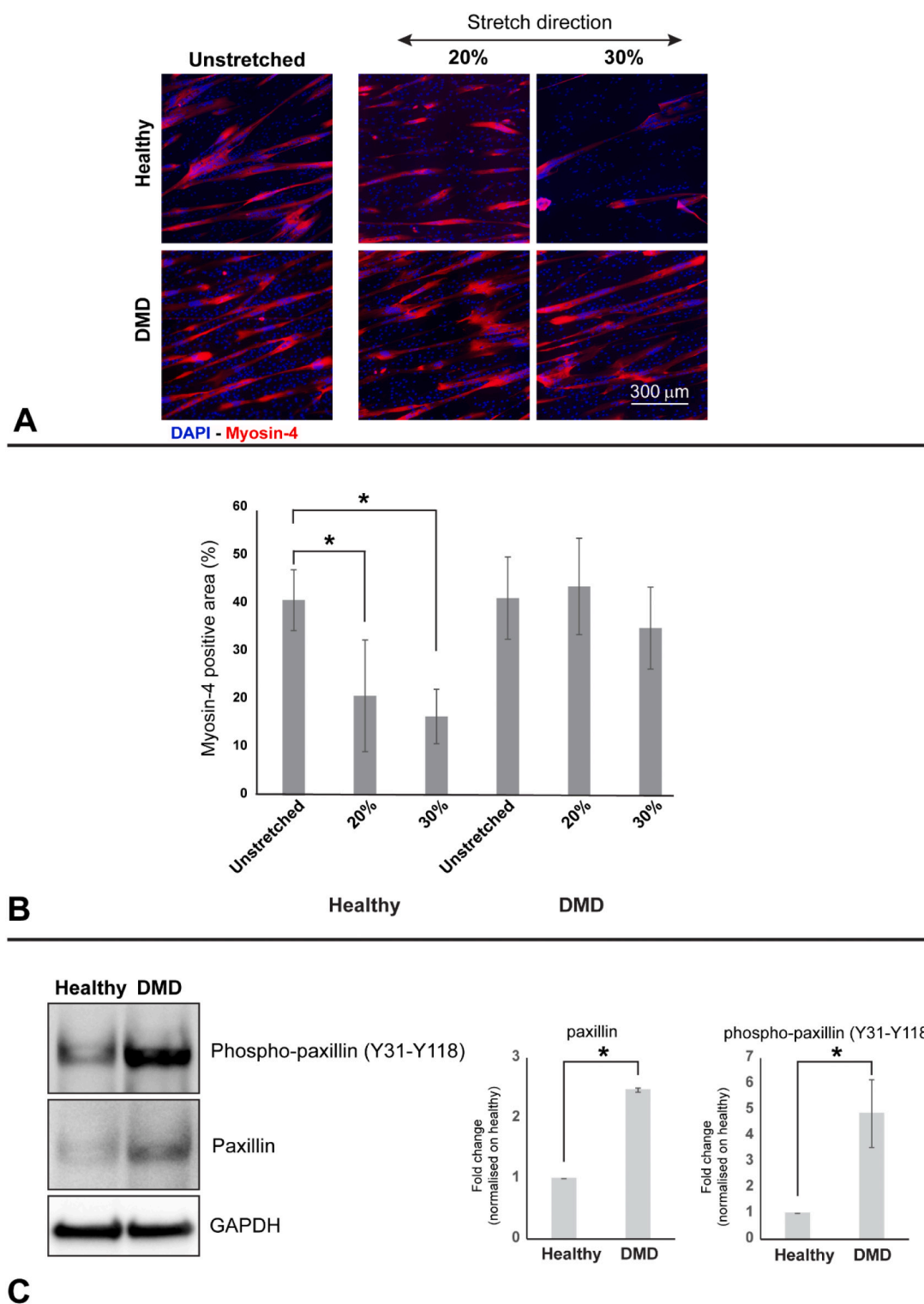


Fig. 7. A) Representative immunofluorescence images of Myosin-4 (red) positive stained healthy and DMD myotubes in the control unstretched culture condition, as well as upon the application of different levels of strain in the stretch direction. Noticeable myotube detachment of cells can be observed, deduced by the lack of these cells present for the healthy myotubes at both levels of stretch; no noticeable change is observed for the DMD myotubes at any level of stretch. B) Plot showing the Myosin-4 positively stained area (%) based on image analysis results. After using Kolomogorov-Smirnov test to determine non-normality of Myosin 4 positive area grouped data, A non-parametric Kruskal-Wallis test with Dunn's multiple comparisons was performed with a $p < 0.05$ and $n > 8$ on the myosin 4 positive area data, which showed that there is a significant change in the Myosin-4 positive area between the healthy unstretched and both stretched conditions. No significant changes were observed between the DMD groups. C) Western blot analysis shows a significantly larger relative amount of phospho-paxillin and total paxillin in the DMD group * $p < 0.05$, $n = 3$ independent experiments (unpaired Student's t -test).

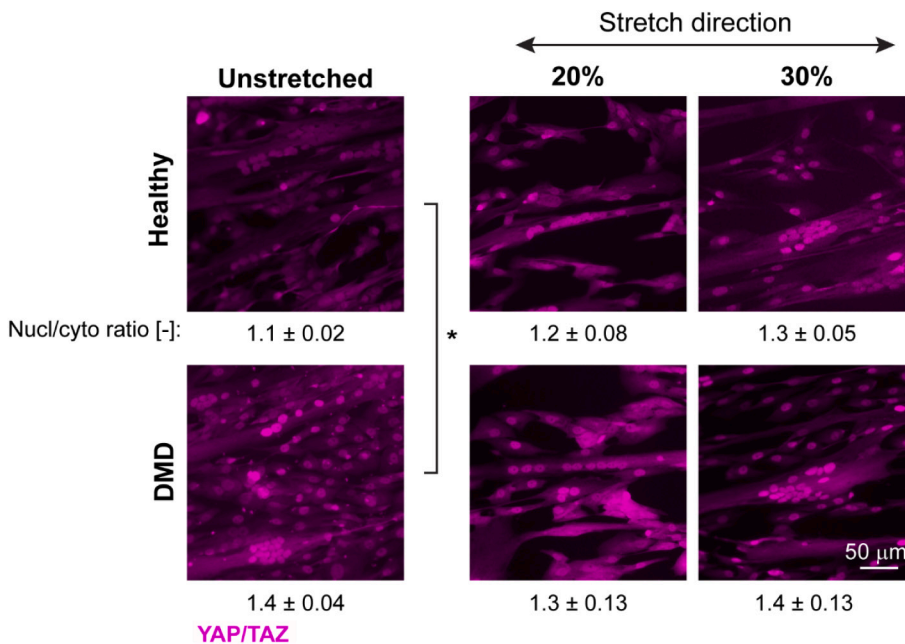


Fig. 8. Representative immunofluorescence images of YAP/TAZ-stained cells in healthy and DMD groups in the control unstretched conditions and upon application of different levels of strain in the stretch direction. Mean \pm standard deviations for the ratio of intensity values between nuclear and cytoplasmic stained signal is displayed under each image. There is a higher basal level of nuclear YAP/TAZ signal for the DMD unstretched condition ($p < 0.05$, Kruskal-Wallis test with Dunn's multiple comparisons). Upon stretching of the healthy group, a slight increase in YAP/TAZ nuclear localization, positively correlated with the level of strain, is detected. For the DMD group, there is no noticeable trend in change of nuclear YAP/TAZ nuclear localization.

presented. Myosin-4 immunofluorescence post-processing of stretched samples revealed a new phenotypic difference in the behavior of the two cell populations. While healthy cells detached from the substrates after stretch, DMD cells did not. This can be ascribed to an alteration in the adhesion dynamics that was previously reported in the *mdx* mouse model *in vivo*³⁰ and confirmed here by western blot analysis of paxillin protein level and activation. It could also be ascribed to an apparent lower stiffness of dystrophic muscle tissue [16] that is also congruent with lower baseline and peak contractile stresses found *in vitro* with DMD myotubes [47]. This lower contractile stress could reduce the forces at the cell-substrate interface below the critical failure point for the cell adhesion. Although the exact reason for cell detachment was not described, this newly identified feature in the mechanoresponse of DMD myotubes is nonetheless of potential interest for screening of clinically relevant drugs using the presented stretch device as an *in vitro* tool. By exploiting a distinguishable difference between a healthy and pathologic cell type (revealed using this device), therapeutic drugs could be easily evaluated for restoration of acute normal mechanoresponses to applied stretch. Given that the device is inexpensive, quick to produce, and simple to use, it could be a promising tool for the validation of potentially disease-relevant targets and the identification and testing of promising candidates for drug development.

Moreover, we compared YAP/TAZ nuclear localization between the two cell types. YAP/TAZ are known sensors for mechanical stimuli, including cell stretch. It was previously reported that in *in vivo* and *ex vivo* models of DMD, YAP/TAZ nuclear signaling was impaired [34]. Our results partially recapitulated the previous literature. A significantly higher basal nuclear localization was observed in DMD compared to the healthy cells, like previous reports [34]. However, in healthy cells we observed a non-significant but increasing trend YAP/TAZ relocalization to the nucleus consistent with the imposed amount of stretch. The lack of statistical significance of YAP/TAZ nuclear relocalization upon stretch of healthy cells can be attributed to the brief timeline of the experiments performed in this study. While current *in vivo* and *ex vivo* DMD models show significant changes of YAP/TAZ nuclear localization after 2 h of stimulation, here, the analysis was performed after a few seconds (overall <5 s). Although it is well accepted that mechanical stimuli are the fastest communication pathway in cells [48], a significant YAP/TAZ nuclear translocation upon mechanical stimuli requires minutes [49]. These observations support that the bistable stretching device can

capture immediate and passive responses to mechanical stretch, even before certain early active downstream pathways can be sufficiently activated such as YAP/TAZ nuclear localization.

Beyond the specific applications presented for the stretching device, the characteristics of this device make it a flexible candidate for various other applications. As demonstrated, the slim profile and open optical path of the device makes it compatible for live-cell imaging since the device can be submerged in a petri-dish with cell culture medium and mounted on a microscope stage. In this study, only instantaneous or short-term effects of stretch were studied, but time-course effects that onset at later timepoints can also be observed by allowing cells to respond or relax to the initial loading for some duration before fixation. Given the biocompatibility of all the materials used for the device and its suitability for placement in an incubator, the set-up can be used for long-term investigations of cell response to applied stretch. Finally, the design for only a uniaxial bistable stretching device was introduced, but through redesign of the 3D-printed compliant mechanism, a variety of substrate deformation states can be created. Multistability can be introduced for evaluation at incremental stretch levels [50,51], and different kinematic configurations of stretch can be imposed (e.g. biaxial). Since many tissues in the body are under a baseline level of tension (e.g. blood vessels, muscle), in a reverse procedure as the one applied in the present work, the device could be used to investigate the loss of tension immediately following traumatic rupture. Furthermore, multistable arrangements of the device are of interest since they would allow testing of intermediate or multiple loading steps.

In conclusion, we present the design of a uniaxial bistable stretching device for adherent cell study applications. A proof-of-principle of the device to elucidate mechanoresponsive effects of stretch was demonstrated by providing evidence of a passive mechanical difference in how healthy and dystrophic myotube cells respond to a rapidly applied stretch. This stretching device is simple, low-cost, and easily modifiable making it a potentially powerful tool for future mechanobiological studies.

CRediT authorship contribution statement

Young Choi: Methodology, Investigation, Formal analysis, Visualization, Data curation, Resources, Software, Writing – original draft, Writing – review & editing. **Giulia Morlino:** Resources, Writing –

review & editing. **Amparo Toboso-Navasa:** Resources, Writing – review & editing. **Raoul Hopf:** Data curation, Software. **Francesca Michela Pramotton:** Investigation, Writing – review & editing. **Anne Bigot:** Resources. **Andrea Taddei:** Resources, Writing – review & editing. **Nikola Cesarovic:** Writing – review & editing. **Volkmar Falk:** Writing – review & editing. **Edoardo Mazza:** Conceptualization, Supervision, Funding acquisition, Writing – review & editing. **Costanza Giampietro:** Conceptualization, Supervision, Funding acquisition, Writing – original draft, Writing – review & editing.

Declaration of competing interest

Authors have no competing interests to declare.

Data availability

Data will be made available on request.

Acknowledgments

The authors want to thank Ute Drechsler (BRNC - Binnig and Rohrer Nanotechnology Center of ETH Zurich) for the assistance in the wafer preparation, Vincent Mouly (Institut de Myologie, Paris, France) for kindly sharing the immortalized human myoblasts, and Jung-Chew Tse (Insitute of Mechanical Systems, ETH, Zurich, Switzerland) for 3D-printing support.

This work was supported by the Swiss National Science Foundation (grant SNF; 205321_188828 to C.G.). Y.C. is supported by EThHeart Initiative operated by ETH Zurich.

Appendix A. Supplementary data

Supplementary data to this article can be found online at <https://doi.org/10.1016/j.bioadv.2022.213134>.

References

- [1] G.B. Blanchard, et al., Tissue tectonics: morphogenetic strain rates, cell shape change and intercalation, *Nat. Methods* 6 (2009) 458–464.
- [2] P.A. Janmey, R.T. Miller, Mechanisms of mechanical signaling in development and disease, *J. Cell Sci.* 124 (2011) 9–18.
- [3] B.W. Benham-Pyle, B.L. Pruitt, W.J. Nelson, Mechanical strain induces E-cadherin-dependent Yap1 and β -catenin activation to drive cell cycle entry, *Science* (80-) 348 (2015), 1024 LP – 1027.
- [4] N.F. Jufri, A. Mohamedali, A. Avolio, M.S. Baker, Mechanical stretch: physiological and pathological implications for human vascular endothelial cells, *Vasc. Cell* 7 (2015) 8.
- [5] W. Zhang, G. Huang, F. Xu, Engineering biomaterials and approaches for mechanical stretching of cells in three dimensions, *Front. Bioeng. Biotechnol.* 8 (2020) 1151.
- [6] S. Landau, S. Ben-Shaul, S. Levenberg, Oscillatory strain promotes vessel stabilization and alignment through fibroblast YAP-mediated mechanosensitivity, *Adv. Sci.* 5 (2018), 1800506.
- [7] H. Ghazizadeh, S. Aravamudan, A review of two-dimensional in vitro cell stretch platforms, *J. Mech. Med. Biol.* 17 (2017), 1730003.
- [8] O. Friedrich, et al., Stretch in focus: 2D inplane cell stretch Systems for Studies of cardiac mechano-signaling, *Front. Bioeng. Biotechnol.* 7 (2019) 55.
- [9] O. Friedrich, et al., Adding dimension to cellular mechanotransduction: advances in biomedical engineering of multiaxial cell-stretch systems and their application to cardiovascular biomechanics and mechano-signaling, *Prog. Biophys. Mol. Biol.* 130 (2017) 170–191.
- [10] A. Livne, E. Bouchbinder, B. Geiger, Cell reorientation under cyclic stretching, *Nat. Commun.* 5 (2014) 3938.
- [11] S.A. Zirbel, K.A. Tolman, B.P. Trease, L.L. Howell, Bistable mechanisms for space applications, *PLoS One* 11 (2016), e0168218.
- [12] D. Ren, et al., Molecular and biomechanical adaptations to mechanical stretch in cultured myotubes, *Front. Physiol.* 12 (2021) 1132.
- [13] P.G. De Deyne, Formation of sarcomeres in developing myotubes: role of mechanical stretch and contractile activation, *Am. J. Physiol. Physiol.* 279 (2000) C1801–C1811.
- [14] D. Duan, N. Goemans, S. Takeda, E. Mercuri, A. Aartsma-Rus, Duchenne muscular dystrophy, *Nat. Rev. Dis. Primers.* 7 (2021) 13.
- [15] S. Puttini, et al., Gene-mediated restoration of Normal myofiber elasticity in dystrophic muscles, *Mol. Ther.* 17 (2009) 19–25.
- [16] T. Uchimura, T. Asano, T. Nakata, A. Hotta, H. Sakurai, A muscle fatigue-like contractile decline was recapitulated using skeletal myotubes from duchenne muscular dystrophy patient-derived iPSCs, *Cell Rep. Med.* 2 (2021), 100298.
- [17] V. DeStefano, S. Khan, A. Tabada, Applications of PLA in modern medicine, *Eng. Regen.* 1 (2020) 76–87.
- [18] B.J. Bachmann, et al., A novel bioreactor system for the assessment of endothelialization on deformable surfaces, *Sci. Rep.* 6 (2016) 38861.
- [19] R. Hopf, et al., Experimental and theoretical analyses of the age-dependent large-strain behavior of sylgard 184 (10:1) silicone elastomer, *J. Mech. Behav. Biomed. Mater.* 60 (2016) 425–437.
- [20] J. Blaber, B. Adair, A. Antoniou, Ncorr: open-source 2D digital image correlation matlab software, *Exp. Mech.* 55 (2015) 1105–1122.
- [21] D. Franco, et al., Accelerated endothelial wound healing on microstructured substrates under flow, *Biomaterials* 34 (2013) 1488–1497.
- [22] K. Mamchaoui, et al., Immortalized pathological human myoblasts: towards a universal tool for the study of neuromuscular disorders, *Skelet. Muscle* 1 (2011) 34.
- [23] P. Bankhead, et al., QuPath: open source software for digital pathology image analysis, *Sci. Rep.* 7 (2017) 16878.
- [24] J.D. Humphrey, in: J.D. Humphrey (Ed.), *Continuum Mechanics BT - Cardiovascular Solid Mechanics: Cells, Tissues, and Organs*, Springer, New York, 2002, pp. 68–106, https://doi.org/10.1007/978-0-387-21576-1_3.
- [25] J.E. Rupert, D.H.A. Jengelle, T.A. Zimmers, In vitro, in vivo, and in silico methods for assessment of muscle size and muscle growth regulation, *Shock* 53 (2020) 605–615.
- [26] A.M. Almonacid Suarez, et al., Topography-mediated myotube and endothelial alignment, differentiation, and extracellular matrix organization for skeletal muscle engineering, *Polymers* 12 (2020).
- [27] M.A. Griffin, et al., Patterning, prestress, and peeling dynamics of myocytes, *Biophys. J.* 86 (2004) 1209–1222.
- [28] H.M. Langevin, et al., Tissue stretch induces nuclear remodeling in connective tissue fibroblasts, *Histochem. Cell Biol.* 133 (2010) 405–415.
- [29] L.M. Hoffman, et al., Mechanical stress triggers nuclear remodeling and the formation of transmembrane actin nuclear lines with associated nuclear pore complexes, *Mol. Biol. Cell* 31 (2020) 1774–1787.
- [30] S. Sen, et al., Upregulation of paxillin and focal adhesion signaling follows dystroglycan complex deletions and promotes a hypertensive state of differentiation, *Eur. J. Cell Biol.* 90 (2011) 249–260.
- [31] X. Cai, K.-C. Wang, Z. Meng, Mechanoregulation of YAP and TAZ in cellular homeostasis and disease progression, *Front. Cell Dev. Biol.* 9 (2021) 1333.
- [32] M. Aragona, et al., A mechanical checkpoint controls multicellular growth through YAP/TAZ regulation by actin-processing factors, *Cell* 154 (2013) 1047–1059.
- [33] J.J. Belanto, et al., Independent variability of microtubule perturbations associated with dystrophinopathy, *Hum. Mol. Genet.* 25 (2016) 4951–4961.
- [34] S.R. Iyer, et al., Differential YAP nuclear signaling in healthy and dystrophic skeletal muscle, *Am. J. Physiol. Physiol.* 317 (2019) C48–C57.
- [35] D.J. Shiowski, J.W. Tashman, A.F. Eaton, G. Apodaca, A.W. Feinberg, 3D printed biaxial stretcher compatible with live fluorescence microscopy, *HardwareX* 7 (2020), e00095.
- [36] C.R. Mayer, P.T. Arsenovic, K. Bathula, K.B. Denis, D.E. Conway, Characterization of 3D printed stretching devices for imaging force transmission in live-cells, *Cell. Mol. Bioeng.* 12 (2019) 289–300.
- [37] S. Toume, A. Gefen, D. Weihs, Printable low-cost, sustained and dynamic cell stretching apparatus, *J. Biomech.* 49 (2016) 1336–1339.
- [38] N.A. Al-Maslami, A.A. Khilan, H.F. Horn, Design of a 3D printed, motorized, uniaxial cell stretcher for microscopic and biochemical analysis of mechanotransduction, *Biol. Open* 10 (2021).
- [39] A.C. Daulagala, in: K. Turksen (Ed.), *A Simple Method to Test Mechanical Strain on Epithelial Cell Monolayers Using a 3D-Printed Stretcher BT - Permeability Barrier: Methods and Protocols*, Springer, US, 2021, p. 247, https://doi.org/10.1007/978-1-4939-9999-9_14.
- [40] A.W. Holle, S. Chao, M.R. Holl, J.M. Houkal, D.R. Meldrum, Characterization of program controlled CO₂ Laser-Cut PDMS channels for Lab-on-a-chip applications, in: 2007 IEEE International Conference on Automation Science and Engineering, 2007, pp. 621–627, <https://doi.org/10.1109/COASE.2007.4341853>.
- [41] S.E. Schneider, et al., Dynamic biophysical responses of neuronal cell nuclei and cytoskeletal structure following high impulse loading, *Acta Biomater.* (2022), <https://doi.org/10.1016/j.actbio.2022.07.002>.
- [42] A.M. Goldyn, P. Kaiser, J.P. Spatz, C. Ballestrem, R. Kemkemmer, The kinetics of force-induced cell reorganization depend on microtubules and actin, *Cytoskeleton* 67 (2010) 241–250.
- [43] H. Wolfenson, et al., A role for the juxtamembrane cytoplasm in the molecular dynamics of focal adhesions, *PLoS One* 4 (2009), e4304.
- [44] M. Fritzsche, A. Lewalle, T. Duke, K. Kruse, G. Charras, Analysis of turnover dynamics of the submembranous actin cortex, *Mol. Biol. Cell* 24 (2013) 757–767.
- [45] N. Wang, J.D. Tytell, D.E. Ingber, Mechanotransduction at a distance: mechanically coupling the extracellular matrix with the nucleus, *Nat. Rev. Mol. Cell Biol.* 10 (2009) 75–82.
- [46] K.N. Dahl, S.M. Kahn, K.L. Wilson, D.E. Discher, The nuclear envelope lamina network has elasticity and a compressibility limit suggestive of a molecular shock absorber, *J. Cell Sci.* 117 (2004) 4779–4786.
- [47] A.P. Nesmith, et al., A human in vitro model of duchenne muscular dystrophy muscle formation and contractility, *J. Cell Biol.* 215 (2016) 47–56.
- [48] S. Na, et al., Rapid signal transduction in living cells is a unique feature of mechanotransduction, *Proc. Natl. Acad. Sci.* (2008), <https://doi.org/10.1073/pnas.0711704105>.

- [49] A. Elsegui-Artola, et al., Force triggers YAP nuclear entry by regulating transport across nuclear pores, *Cell* 171 (2017) 1397–1410.e14.
- [50] L. Li, B. Li, G. Chen, A non-transit fully compliant tristable mechanism capable of direct switching between every two stable positions, *Mech. Syst. Signal Process.* (2021), 108597, <https://doi.org/10.1016/j.ymssp.2021.108597>.
- [51] G. Chen, Q.T. Aten, S. Zirbel, B.D. Jensen, L.L. Howell, A tristable mechanism configuration employing orthogonal compliant mechanisms, *J. Mech. Robot.* 2 (2009).